The Isothermal Oxidation of a New Polycrystalline Turbine Disk Ni-Based Superalloy at 800 °C and Its Modification with Pre-oxidation

J.W.X. WO, H.T. PANG, A.S. WILSON, M.C. HARDY, and H.J. STONE

Ni-based superalloys with enhanced oxidation resistance at high temperatures are crucial for next-generation gas turbine engines. A new polycrystalline Ni-based superalloy (C19) that combines improved microstructural stability with environmental resistance has been developed. Its oxidation resistance has been determined through measurements of the specific mass change and morphological evolution of the formed oxides following furnace exposures at 800 °C in air for up to 1000 hours; the results of which were benchmarked against Nimonic 105. C19 showed hybrid Type II/Type III behavior as a marginal Al_2O_3 former and performed similarly to established superalloys at 750 °C. The Wagner model for the transition from internal to external oxide formation predicted that C19 should form a continuous Al_2O_3 scale at higher temperatures. A pre-oxidation treatment at 1100 °C for 1 hour was, therefore, selected and shown to dramatically improve the oxidation resistance during subsequent exposure at 800 °C. Oxide cross-sectional analysis showed that C19 formed a continuous and protective Al_2O_3 scale after the pre-oxidation treatment, whereas Nimonic 105 retained discontinuous Al_2O_3 finger-like intrusions beneath a Cr_2O_3 overscale.

I. INTRODUCTION

GLOBAL efforts to reduce emissions and increase sustainability are driving next-generation aeroengine designs to more aggressive service temperatures. New Ni-based superalloys with enhanced resistance to environmental attack must consequently be developed to tolerate the increased oxidation rates that are expected at these higher service temperatures. Oxidation resistance in Ni-based superalloys is typically achieved by alloy compositions that promote the rapid formation of a continuous surface oxide layer that prevents further oxidation damage. Specifically, Al and Cr additions are favored as they produce adherent and protective scales of alumina (Al_2O_3) and chromia (Cr_2O_3). Giggins and Pettit[1] proposed that Ni–Cr–Al-containing alloys can be divided into one of three groups depending on their oxidation behavior: Type I alloys form a non-protective external scale of NiO with a discontinuous sub-scale of Al_2O_3 and Cr_2O_3 intrusions; Type II alloys form a continuous external scale of Cr_2O_3 with sub-scale discontinuous Al_2O_3 intrusions; and Type III alloys form a continuous external scale of Al_2O_3. It was also noted[1] that alloys which form a continuous scale of Al_2O_3 underneath an external Cr_2O_3 scale can also be classified as Type III.

Current temperatures experienced by turbine disks in gas turbine engines typically do not exceed 750 °C,[2] resulting in many commercial polycrystalline superalloys for turbine disks relying on forming a Cr_2O_3 scale (Type II) to achieve the required oxidation resistance. However, Cr_2O_3 loses efficacy as a protective oxide at higher temperatures as volatile oxide species are formed, which reach comparatively high vapor pressures.[3] It is well established that Al_2O_3 provides a more stable and protective oxide layer at higher temperatures than Cr_2O_3, making it a more attractive option for components that experience such conditions in service.[4] Therefore, the development of polycrystalline superalloys that form protective scales of Al_2O_3 (Type III) instead of Cr_2O_3 could offer benefits for future more fuel-efficient gas turbine engines.

In polycrystalline superalloys, the formation of Al_2O_3 typically occurs as discontinuous, finger-like intrusions underneath a compact surface scale of Cr_2O_3 and has been widely documented.[5,6] While the formation of discontinuous Al_2O_3 intrusions is a common occurrence, their morphological evolution shows significant

J.W.X. WO, H.T. PANG, A.S. WILSON, and H.J. STONE are with the Department of Materials Science and Metallurgy, University of Cambridge, 27 Charles Babbage Road, Cambridge, CB3 0FS, UK. Contact e-mail: hjs1002@cam.ac.uk M.C. HARDY is with the Rolls-Royce plc, PO box 31, Derby, DE24 8BJ, UK.

variability depending on the overall alloy composition, alloy surface condition, and operating temperature. For example, one study investigated the oxidation of several commercial polycrystalline Ni-based superalloys from 750 °C to 1000 °C and showed that Al only formed internal oxides, while Cr and Ti formed external oxides that resulted in complex multi-layered oxide scales.[5] Similar results were observed[7] in alloys of varying Al, Co, Cr, and Ti concentrations where internal Al_2O_3 formed, with significant layers of Co, Cr, and Ti-based oxides on the external surface. The study also showed that the capacity of the alloys to form a continuous Cr_2O_3 layer could be improved by decreasing Co or Ti and increasing Al or Ni concentrations. Such enrichment of Cr and Ti in the external scale has been observed consistently in multiple studies of the oxidation of the Ni-based superalloy RR1000 at 700 °C to 800 °C.[8] In these studies, the presence of discontinuous, intergranular veins of Al_2O_3 accompanied by TiO_2 formation over a relatively porous Cr_2O_3 scale led to significant oxidation damage that extended up to 10 to 20 μm into the substrate. It has also been shown that Cr and Al work synergistically to form a multi-layered oxide scale, with the former promoting the formation of the latter.[9] These studies suggest that Cr and Al concentrations must be carefully selected to achieve optimal environmental resistance.

Traditional alloy development has relied primarily on empirical methods. However, this is becoming increasingly impractical given the complex compositions of the latest Ni-based superalloys. Computational methods[10,11] have been consequently used to predict the tendency of an alloy composition to preferentially form a protective oxide (e.g., Cr_2O_3 or Al_2O_3). Such models often make use of established physical relationships describing elemental interdiffusion and oxidation. The original relationship proposed by Darken assumed that oxygen diffusion is hindered by the gradual establishment of oxide particles in an internal oxidation zone.[12] Wagner[13] extended Darken's theory by assuming that the transition from internal to external oxide formation will occur if the solute concentration is sufficiently high such that the volume fraction of the internal oxides is greater than a critical volume fraction. This enabled a mathematical expression to be derived for the minimum solute concentration required for external oxidation in a binary A–B system:

$$N_B^o = \left[f\left(\frac{V_m}{V_{ox}}\right) \pi \frac{N_O^S D_O}{2vD_B} \right]^{\frac{1}{2}}, \quad [1]$$

where N_B^o is the minimum critical concentration of solute B required for external oxidation (mol fraction), f is the volume fraction of internal oxide, V_m and V_{ox} are the respective molar volumes of the alloy and oxide (cm^3/mol), N_O^S is the solubility of oxygen in the alloy (mol fraction), D_O is the diffusivity of oxygen in the alloy (cm^2/s), D_B is the diffusivity of the solute B in the alloy (cm^2/s), and v is the stoichiometric ratio of oxygen to solute atoms B (i.e., 1.5 for Al_2O_3). Rapp[14] experimentally verified Wagner's equations in a Ag-In

system at 550 °C and determined the critical volume fraction f to be 0.3. The study proposed that the choice of f is highly dependent on alloy composition, highlighting the non-universal and simplifying assumptions of Wagner's theory. Nevertheless, the value of $f = 0.3$ has been widely used. Wagner's theory was also experimentally assessed in Ni–Al alloys[15] and shown to underpredict the Al concentrations required for Al_2O_3 formation. However, the theory was shown to be in reasonable agreement with experimental Al concentrations in the case of ternary Ni–Cr–Al alloys at 1200 °C.

As the minimum critical concentration of solute B required for external oxidation varies with temperature, it is in principle possible to switch from internal to external oxidation by changing temperature. To exploit this phenomenon, pre-oxidation treatments have been considered whereby alloys are subjected to a carefully chosen regimen of temperature, time, and atmosphere to promote the formation of a desired oxide for protection.[16] However, there are relatively few studies that have used this technique to achieve the same effect in Ni-based superalloys. In one study,[17] the authors applied a pre-oxidation treatment at 800 °C for 140 hours to Nimonic 95 and subsequently observed excellent oxidation resistance at 1000 °C. However, their pre-oxidized samples still exhibited Type II behavior[1] and required at least 24 hours of further exposure at 1000 °C to achieve a continuous Al_2O_3 layer underneath the Cr_2O_3 overscale. Another work examined the effect of pre-oxidation treatments in air and H_2O-Ar environments at 950 °C in commercial Ni-based superalloys[18] in which the authors observed a wide range of Type II and Type III oxidation behaviors and found that pre-oxidation treatment in H_2O-Ar was detrimental to protective oxide formation when compared to pre-oxidation in air.

It is clear from the literature that the formation of a continuous Al_2O_3 scale in polycrystalline Ni-based superalloys where the volume fraction of the γ' phase must be restricted to aid processability is challenging. By examining the general compositional trends in Cr_2O_3-forming and Al_2O_3-forming commercial alloys, a new polycrystalline Ni-based superalloy has been created and studied (C19)[19,20] for applications that require mechanical performance up to 800 °C. The present study outlines the oxidation behavior of C19 for between 6 and 1000 hours at 800 °C. The results have been benchmarked against Nimonic (NIM) 105, an established commercial alloy with favorable oxidation resistance, and compared with data from previous studies. In addition, the application and ability of a pre-oxidation treatment to C19 and NIM 105 to encourage the formation of a continuous Al_2O_3 scale have been investigated.

II. EXPERIMENTAL METHODOLOGY

A. Materials

The compositions of C19 and NIM 105 are outlined in Table I. The composition of C19 was designed by

Table I.   Composition of the Investigated Alloys (At. Pct)

Element	C19 (At. Pct)	NIM 105 (At. Pct)	Element	C19 (At. Pct)	NIM 105 (At. Pct)
Al	9.41	9.78	Si	—	0.12
Co	19.25	18.87	Ta	1.63	—
Cr	13.18	15.78	Ti	1.91	1.48
Cu	—	0.06	W	1.25	—
Fe	—	0.10	Zr	0.06	0.07
Mn	0.59	0.02	B	0.20	0.03
Mo	1.79	2.93	C	0.15	0.60
Nb	1.02	—	Ni	49.56	50.16
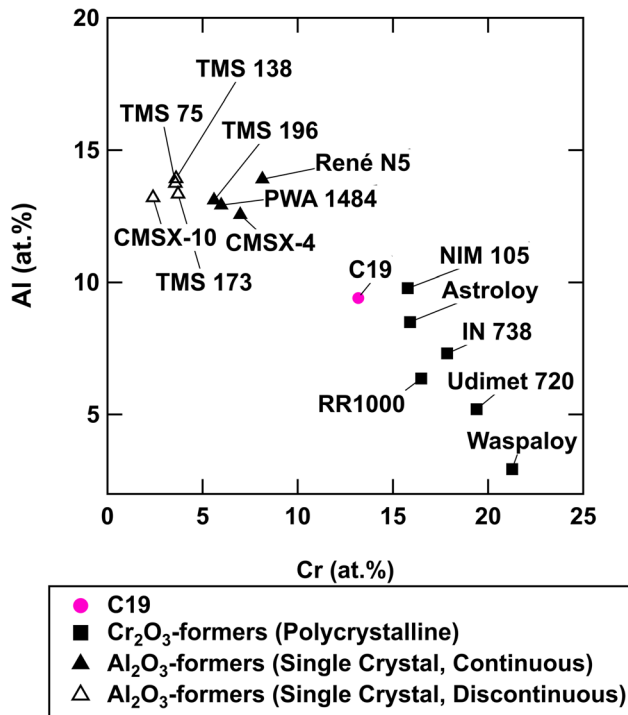
Fig. 1—Plot of Al vs Cr concentrations (at. pct) for various commercial alloys. The solid squares, solid triangles, and hollow triangles denote known polycrystalline Cr_2O_3-forming alloys, continuous Al_2O_3-forming single-crystal alloys, and discontinuous Al_2O_3-forming single-crystal alloys, respectively. Data taken from sources[5,21,22,23,24].

analyzing the Al and Cr concentrations (at. pct) of various known commercial alloys (Figure 1). The Cr concentration of C19 was chosen to be approximately 2.60 at. pct lower than NIM 105 to improve phase stability. The Al concentration in C19 (9.41 at. pct) was kept approximately equivalent to NIM 105 (9.78 at. pct). It can be seen in Figure 1 that these adjustments to the Cr and Al concentrations place C19 in the intermediate region between alloys that form Cr_2O_3 or Al_2O_3 oxide scales.

The thermodynamic modeling software, *Thermo-Calc 2021b*, was used to determine the appropriate concentrations of several common alloying additions for minimum formation of topologically close-packed (TCP) phases and maximum alloy strength. To this end, the concentration of Al in C19 (9.41 at. pct) was chosen to be slightly lower than but approximately

similar to NIM 105 (9.78 at. pct) to maintain an acceptable balance of γ' formation and oxidation resistance. Mo was added for solid-solution strengthening but at a reduced concentration (by 1.14 at. pct) compared to NIM 105. Fe and Si were removed completely due to their propensity for forming Laves phases.[25] Nb and Ta were judiciously added to promote the formation and strengthening of the γ' phase. A relatively high concentration of Co (19.25 at. pct) was included for solid-solution strengthening and minimization of stacking fault energy.[26] A slightly higher concentration of Ti was chosen to promote γ' formation and increase the APB energy[27] while being sufficiently low to avoid detrimental oxidation effects. A small concentration of W (1.25 at. pct) was included to improve solution strengthening and creep resistance while minimizing TCP phase formation. A comparatively high concentration of Mn was included compared to NIM 105 for enhanced oxidation resistance. The concentration of boron was selected to be 0.2 at. pct for improved grain boundary strengthening while carbon content was minimized. The concentration of Zr was maintained at a similar level to NIM 105.

Samples of C19 were produced by powder metallurgy techniques culminating in hot-isostatic pressing (HIP) at 1107 °C and 100 MPa for 4 hours. The C19 samples were super-solvus solutioned at 1190 °C for 1 hour, followed by air cooling. Subsequently, the materials were subjected to consecutive precipitate aging heat treatments at 843 °C and 800 °C for 2 hours at each temperature.

NIM 105 samples were obtained from the base of a partially completed high-pressure compressor blade. The NIM 105 samples were solutioned at 1150 °C for 4 hours, followed by consecutive precipitation aging heat treatments at 1030 °C and 700 °C for 16 hours at each temperature with air cooling between the two aging heat treatments.

B. *Thermo-Gravimetric Analysis*

Thermo-Gravimetric Analysis (TGA) measurements were performed using a Setaram Setsys Evolution 18 apparatus to study the specific mass change associated with oxidation for both C19 and NIM 105. The TGA experiments were carried out at 800 °C for 100 hours in air. The test temperature of 800 °C was chosen as this represents the upper limit of intended operating temperatures for C19 in service. Samples for TGA analysis

were prepared as rectangular plates with approximate dimensions of $20 \times 10 \times 1$ mm. The final sample dimensions were measured using a digital vernier scale to allow specific mass changes to be accurately calculated from associated mass change data. All faces and sides of the plates were polished to a 1 μm diamond finish. Before the TGA experiments, samples were cleaned in acetone followed by ethanol in an ultrasonic bath and dried for at least 24 hours in a drying cabinet. During the heating process, the sample was first heated from 20 °C to 200 °C at 10 K/min and held for 10 minutes to stabilize. The sample was then heated from 200 °C to 775 °C at 20 K/min. To avoid overshooting the target temperature, the sample was heated from 775 °C to 800 °C at 5 K/min. During the cooling process, the sample was cooled from 800 °C to 20 °C at 35 K/min.

C. Furnace Exposure Experiments

Furnace exposure experiments were carried out to study the evolution of oxide morphologies as a function of time. Samples of C19 and NIM 105 used in these experiments were approximately $10 \times 10 \times 2$ mm rectangular plates, polished to a 1 μm diamond finish. The samples were individually exposed to air at 800 °C for 6, 24, 96, 312, 600, and 1000 hours in a Carbolite CWF1100 laboratory furnace.

D. Pre-oxidation Experiments

To suppress the mass changes observed during TGA experiments, attempts were made to modify the surface condition of samples by forming a partial/fully protective Al_2O_3 oxide layer prior to further TGA experiments. In Ni-based superalloys, the establishment of Cr_2O_3 tends to form relatively quickly[1] and reduces the ingress of oxygen. This slows down the oxidation kinetics, allowing sufficient time for Al to diffuse to the surface to form Al_2O_3 underneath the Cr_2O_3 scale. However, at relatively low temperatures (< 1000 °C), Al diffusion is not rapid enough for this process to occur,[28] resulting in oxygen diffusing further into the substrate and reacting with Al before it reaches the oxide–metal interface. This results in the Al_2O_3 "finger-like" intrusions. Increasing the temperature is expected to accelerate the kinetics such that the diffusion of Al is fast enough to form a continuous layer of Al_2O_3 (Type III behavior). Guided by calculations of the critical concentration of Al required to promote an external Al_2O_3 scale using the Wagner criterion, as detailed in Sections II–F, a pre-oxidation treatment of 1 hour at 1100 °C was, therefore, chosen.

Samples of C19 and NIM 105 were prepared in the same manner as described above to produce TGA samples. The pre-oxidation of the test samples was carried out in situ in the TGA equipment at 1100 °C for 1 hour in air before cooling to ambient temperature. During the heating process, the sample was first heated from 20 °C to 200 °C at 10 K/min and held for 10 minutes to stabilize. The sample was then heated from 200 °C to 300 °C at 20 K/min and 300 °C to

1075 °C at 80 K/min. To avoid overshooting the target temperature, the sample was heated from 1075 °C to 1100 °C at 5 K/min. During the cooling process, the sample was cooled from 1100 °C to 20 °C at 35 K/min. To assess the effects of the pre-oxidation treatment on the oxidation behavior at 800 °C, the samples were subsequently subjected to TGA measurements at this temperature for 100 hours using the same heating and cooling ramps outlined in Section II–B. The oxidized samples were sectioned post-test to investigate the effects of the pre-oxidation on oxide morphologies.

E. Oxide Analyses

X-ray diffraction (XRD) data were acquired to detect and identify surface oxides on selected samples using a Bruker D8 ADVANCE fixed sample X-ray diffractometer fitted with a LynxEye EX position-sensitive detector. A standard program (fixed illuminated length) was used to irradiate the sample over a 2θ range of 10 to 134 deg with a step size of 0.02 deg and a dwell time of 1.5 s/step.

Samples for oxide examination were sectioned with a precision saw utilizing a SiC blade, using a low-impact dry-cut method to minimize potential damage and preserve oxide layers on the sample surfaces. The sectioned samples were mounted in phenolic resin and subsequently ground down by at least 1 mm using SiC-grinding papers to ensure the prepared oxide cross sections were free from potential damage due to cutting. Samples were then polished to a 0.06 μm colloidal silica suspension finish.

Microstructural examination of the polished cross sections was carried out in a Zeiss GeminiSEM 300 scanning electron microscope (SEM) operated at 20 kV and a working distance of approximately 8.5 mm. The instrument was also equipped with an Oxford Instruments energy dispersive X-ray (EDX) detector to facilitate compositional analyses of microstructural features. Oxide cross sections were examined in both secondary electron (SE) and backscattered electron (BSE) modes. Where required, EDX elemental concentration maps of the alloy cross sections were acquired alongside SEM micrographs.

Thickness measurements of the Cr_2O_3, Al_2O_3, internal oxidation products, and γ'-depleted zones were obtained by analyzing SEM images using the image analysis software ImageJ. Thickness measurements of each feature were obtained from 5 uniformly spaced sampling lines in a representative image each covering an area of approximately 11 μm $\times$ 8.5 μm. A total of three representative images were analyzed for a given sample resulting in 15 measurements for each feature, from which standard errors were calculated. Where undulating non-planar surfaces were observed, the thicknesses were measured perpendicular to the surfaces as much as possible. In all samples, the internal oxides were interpreted to be the discontinuous intergranular Al_2O_3 fingers that formed beneath the external scale. If internal products were observed within approximately $\pm$ 1 μm of one of the 5 sampling lines but otherwise not included, the sampling line would be

shifted to include the internal products. The total depth of oxidation damage was defined as the sum of the individual thicknesses of the Cr_2O_3, Al_2O_3, internal oxidation products, and γ'-depleted zones.

F. Wagner Model for Transition from Internal to External Oxidation

Equation [1] is used to calculate the minimum critical concentration of Al required to form an external layer of Al_2O_3. To this end, the approaches that were undertaken to calculate each parameter in Eq. [1] and the procedures are outlined herein. The use of Eq. [1] necessitates the assumption of a binary A–B system. While the investigated alloys are multi-component systems, Cr and Al were assumed to be the primary oxidizing elements within a predominantly Ni-based system. In addition, no external scale was assumed to be initially present, following the assumptions made by Wagner.[13]

The thermodynamic modeling software *Thermo-Calc 2021b* was used to calculate the molar volumes, V_m (cm^3/mol), of the investigated alloys at 800 °C using the TCNi8 v8.2 database. The oxide molar volumes, V_{ox}, of Al_2O_3 were calculated from standard density and molecular weight values from textbook references[29] to be 25.575 cm^3/mol. By approximating the bulk concentration as Ni, the oxygen solubility, N_O^S, and the diffusion coefficient of oxygen in the alloy, D_O (cm^2/s), were calculated with formulations from Park and Altstetter[30]:

$$N_O^S = 8.3 \cdot \exp\left[\frac{-55\frac{kJ}{mol}}{RT}\right], \qquad [2]$$

$$D_O = 1.7 \times 10^{-5} \cdot \exp\left[\frac{-90\frac{kJ}{mol}}{RT}\right], \qquad [3]$$

where R is the universal gas constant (J/mol K), and T is the temperature (K). As a reference, the value of D_B (cm^2/s) of Al in solid Ni from 800 °C to 970 °C was also calculated based on the formulation by Allison and Samelson[31]:

$$D_B = 1.1 \cdot \exp\left[\frac{-249\frac{kJ}{mol}}{RT}\right], \qquad [4]$$

where R is the universal gas constant (J/mol K), and T is the temperature (K). The diffusivities D_O and D_B were assumed to be independent of other elements present. For comparison, the values of D_B in the alloys were also calculated in *Thermo-Calc 2021b* with the TCNi8 v8.2 and MOBNi3 v3.2 databases. By setting the diffusing element to Al, the reference element to Ni, and the gradient element to each component in the alloy, the diffusion coefficients of Al with reference to Ni with respect to other alloy components were computed. The total diffusivity of Al was taken as the sum of these individual diffusion coefficients. The value of the stoichiometric ratio of oxygen to Al atoms in Al_2O_3, v, was

taken to be 1.5. The volume fraction of internal oxide, f, was selected to be 0.3, following the work of Rapp.[14] Despite being alloy dependent, a value of 0.3 has been previously shown to be reasonably accurate for alloys of the type considered through the combined work of Nesbitt[15] and Pettit.[32] Notably, a more recent study[33] provided a more rigorous mathematical treatment for the calculation of f, but the method showed a tendency to overestimate the value when compared to published experimental measurements of f.

III. RESULTS

A. Thermo-Gravimetric Analysis Measurements

The specific mass changes recorded using TGA for C19 and NIM 105 during isothermal oxidation at 800 °C for 100 hours are presented in Figure 2. The specific mass change of NIM 105 showed a comparatively rapid increase within the first 10 to 15 hours. Similarly, the curve for C19 showed an appreciable specific mass change within the first 20 hours, where it achieved approximately half of its final observed specific mass change. The final specific mass changes of NIM 105 and C19 were 0.20 mg/cm^2 and 0.08 mg/cm^2, respectively, after 100 hours at 800 °C.

In order to determine the oxidation behavior of the alloys, the results were fitted to a generalized form of the classical power law equation:

$$(\Delta m)^n = k_n t, \qquad [5]$$

where Δm is the specific mass change (mg/cm^2), t is time (h), n is the mass gain exponent, and k_n is the oxidation rate constant (mg^n/cm^{2n}h). Parabolic oxidation behavior is indicated by an $n \approx 2$ while "sub-parabolic" and "super-parabolic" behavior are characterized by $n < 2$ and $n > 2$, respectively. The TGA data for both the baseline experiment (800 °C for 100 hours) and pre-oxidation treatment (1100 °C for 1 hour) were fitted with Eq. [5] using the MATLAB Curve-Fitting Tool—the fitted coefficients are given in Table II. The 95 pct confidence bounds on the fitted coefficients were also computed with the MATLAB Curve-Fitting Tool using
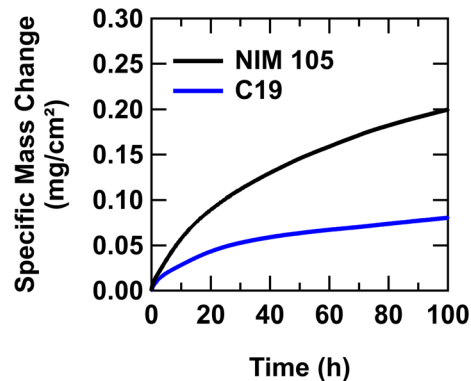

Fig. 2—TGA specific mass change curves for C19 and NIM 105 during oxidation at 800 °C for 100 hours in air.

Table II. Values of n and k_n from Eq. [5] Determined for C19 and NIM 105 for the Baseline Experiment (800 °C for 100 h) and Pre-oxidation Treatment (1100 °C for 1 h) with 95 Pct Confidence Bounds in Parentheses

Sample	800 °C/100 h		1100 °C/1 h	
	C19	NIM 105	C19	NIM 105
n	2.423 (2.416, 2.431)	1.915 (1.912, 1.918)	1.611 (1.606, 1.616)	1.983 (1.973, 1.992)
k_n (mg^n/cm^{2n}h)	2.348×10^{-5} (2.303, 2.393×10^{-5})	4.812×10^{-4} (4.784, 4.839×10^{-4})	0.3067 (0.3051, 0.3083)	0.1933 (0.1913, 0.1952)

Student's cumulative t-distribution function and are presented in parentheses in Table II.

B. *Surface Morphology and XRD Analysis*

SE SEM images of the surface of C19 after oxidation at 800 °C for 1000 hours are shown in Figure 3. In these images, C19 shows uniform oxide formation on the surface with relatively small grains. No regions showing differential oxidation behavior were observed. At higher magnification, the oxide crystals exhibit a plate-like morphology with no apparent preference for orientation. No evidence of surface cracking was observed in the surface SE images.

The XRD diffractogram obtained from the surface oxide scale of C19 after exposure at 800 °C for 1000 hours is shown in Figure 4. Strong diffraction peaks corresponding to the γ and γ' phases in C19 could be identified, which are expected and confirmed with subsequent SEM cross-sectional examination. Peaks associated with the presence of Cr_2O_3, Al_2O_3, TiO_2, $NiCr_2O_4$, and $MnCr_2O_4$ oxides were also identified. It was not possible to unambiguously identify the additional small peak at approximately 16.8 deg 2θ.

C. *Cross-Sectional Oxide Analysis*

The BSE cross-sectional images and associated EDX elemental concentration maps for Cr, Al, Ni, Mn, and Ti obtained from C19 following exposure at 800 °C for 1000 hours are presented in Figure 5. A solid scale of Cr_2O_3 was observed on the surface of the alloy, which appeared mid-gray in BSE imaging. Dark-contrast intrusions were observed beneath this scale, which were associated with high Al content, and were, therefore, determined to be Al_2O_3. The presence of Mn and Ti was also detected in the external oxide layer, overlapping with regions of high Cr concentration. Smaller regions enriched with Ti were also observed deeper into the alloy. These were not associated with increased oxygen content.

BSE images of cross sections of C19 after exposures at 800 °C in air for 6, 24, 96, 312, 600, and 1000 hours are presented in Figure 6 alongside the EDX elemental concentration maps of Cr and Al. The temporal evolution of the oxide scale on C19, shown in Figure 6, exhibits a clear and gradual establishment of a continuous layer of Cr_2O_3 that is visible at 6 hours of exposure. After 96 hours, Al_2O_3 precipitates can be identified as a semi-continuous layer underneath the Cr_2O_3 layer and continue to extend into the alloy substrate with further time at temperature. After 600 hours, a relatively dense layer of Cr_2O_3 formed on the surface, but this did not show appreciable thickening after 1000 hours. The depth of the Al_2O_3 fingers after 1000 hours reached a limiting value of ~ 1 to 2 μm and total oxidation damage depths of up to ~ 5 μm were observed.

The mean thicknesses of the Cr_2O_3 (continuous), Al_2O_3 (semi-continuous, where present), internal products (including discontinuous Al_2O_3), and γ'-depleted zone layers are shown in Figure 7 for C19. The results
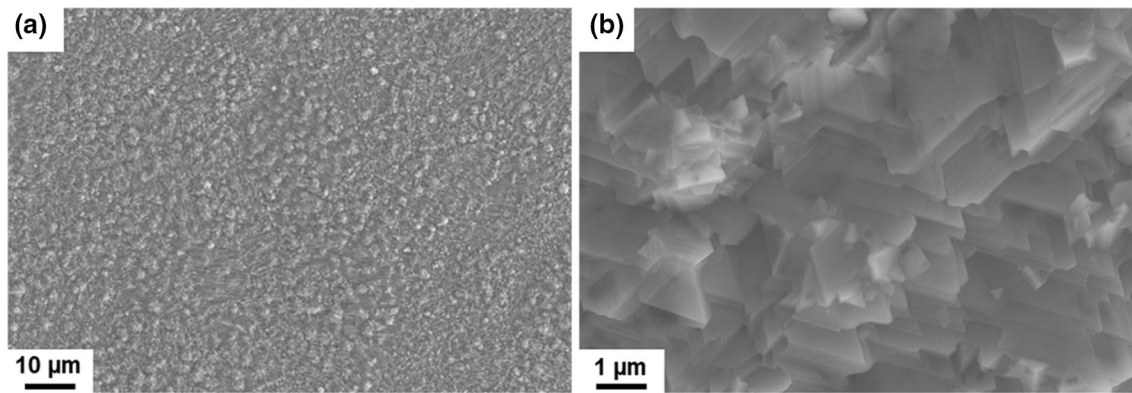
Fig. 3—Representative SE SEM images of oxidized surfaces on C19 at lower (*a*) and higher (*b*) magnification following exposure at 800 °C for 1000 h.
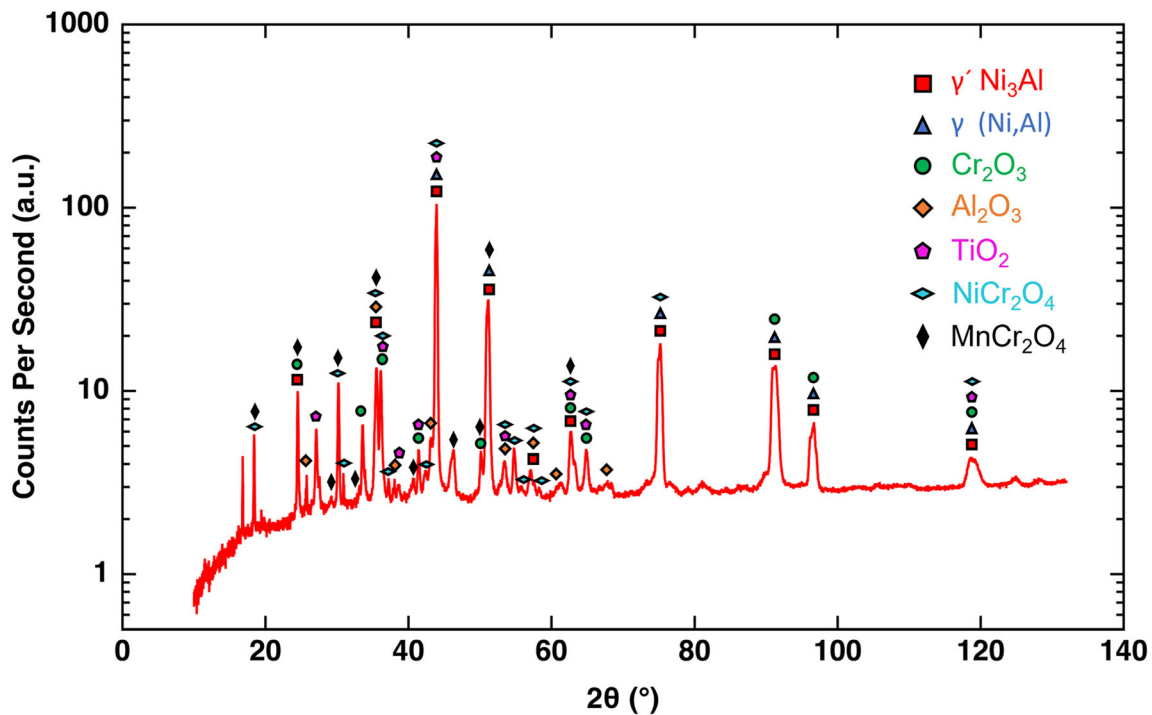

Fig. 4—X-ray diffractogram from the surface of C19 following exposure in air at 800 °C for 1000 h. The horizontal axis displays the angle 2θ, and the vertical axis plots the intensities as Counts Per Second (CPS) in arbitrary units (a.u.). The legend outlines the various identified phases (oxides) as unique symbols.

show a gradual increase in the thicknesses of the Cr_2O_3 layer, internal products, and γ'-depleted zones. The thickness of the semi-continuous Al_2O_3 layer remains thin with increasing exposure time, with Al_2O_3 formation appearing to be dominated by the discontinuous growth of the Al_2O_3 intrusions into the substrate. These intrusions increase in length from under 1 μm to approximately 1.5 μm over the range of times studied. Overall, the total depth of the oxidation damage reaches approximately 3.3 μm in thickness after 1000 hours of exposure. These results are consistent with C19 being a Type II oxide-forming alloy. However, the formation of a near-continuous Al_2O_3 layer suggests that it is close to Type III behavior under these conditions.

D. *Wagner Model Results*

To assess whether a continuous Al_2O_3 scale may be expected during oxidation of C19, calculations were made using the Wagner Model for the transition from internal to external Al_2O_3 scale formation, Eq. [1]. The oxygen solubility, oxygen diffusivity, Al diffusivity in solid Ni, and the theoretical minimum critical concentration of Al (at. pct) required for external oxidation of C19 at 800 °C were calculated with Eqs. [2] through [4] and presented in Table III alongside the associated variables used in the equations. The Wagner Model predicted that a minimum N_B^o of 11.5 at. pct is required for external Al_2O_3 formation at 800 °C. This is above the concentration of Al in the alloy of 9.4 at. pct. As
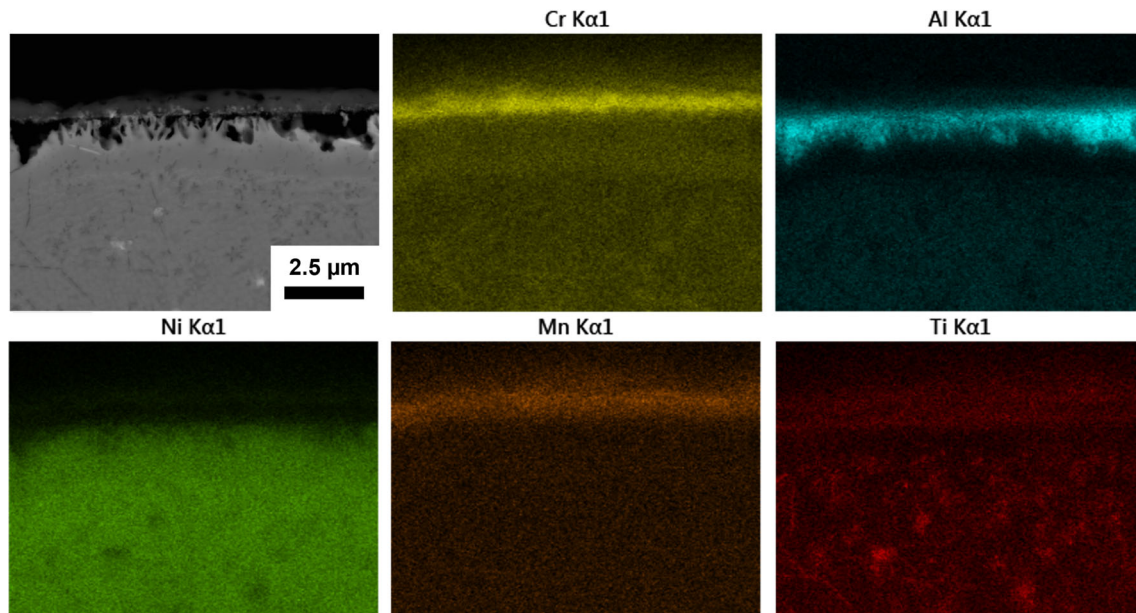
Fig. 5—Cross-sectional BSE SEM image (top left) and corresponding EDX elemental concentration maps of C19 following oxidation in air at 800 °C for 1000 h.

such, a continuous Al_2O_3 scale is not expected to form at this temperature.

Using the same approach, the minimum concentrations of Al required for external Al_2O_3 scale formation at higher temperatures were calculated. At 900 °C, 1000 °C, and 1100 °C, external Al_2O_3 scales were predicted to form with Al concentrations in the alloy of approximately 7.0, 4.6, and 3.2 at. pct, respectively. However, it is noted that the diffusivity of Al used in these calculations was only measured in the temperature range 800 °C to 970 °C.[31] Similarly, the oxygen solubility was determined from 800 °C to 1000 °C and the oxygen diffusivity from 850 °C to 1400 °C.[30] As such, the predicted values for the critical Al concentrations at these higher temperatures are in the extrapolation regime and must be treated with caution. However, recognizing that a transition in behavior may occur with increasing temperature in C19, it was anticipated that a continuous Al_2O_3 scale could be promoted by a short duration pre-oxidation exposure at higher temperature. To study this effect, a pre-oxidation temperature of 1100 °C for 1 hour was selected.

E. Pre-oxidation Results

The specific mass changes recorded using TGA for C19 and NIM 105 during the pre-oxidation treatment of 1100 °C for 1 hour are presented in Figure 8. The pre-oxidation treatment resulted in a substantial increase in the specific mass changes of C19 and NIM 105 compared to the baseline experiment at 800 °C, with respective final specific mass changes of approximately 0.45 and 0.42 mg/cm². A potential inflection point is observed at 0.5 hour in the specific mass change data for C19 while NIM 105 maintains a relatively smoother profile.

The coefficients from fitting Eq. [5] to the specific mass change data for the samples during pre-oxidation for both C19 and NIM 105 are presented in Table II and compared with the baseline experiment. These show substantially higher k_n values than those obtained at 800 °C. Parabolic behavior was still observed for NIM 105 during the oxidation at 1100 °C, although C19 exhibited sub-parabolic kinetics.

The BSE cross-sectional images and EDX elemental concentration maps for Al and Cr obtained from the C19 and NIM 105 samples following pre-oxidation at 1100 °C for 1 hour are presented in Figure 9. A continuous layer of Al_2O_3 could be clearly observed on the surface of the C19 alloy. In contrast, a continuous layer of Cr_2O_3 was observed on the surface of the NIM 105 alloy with discontinuous Al_2O_3 intrusions directly underneath.

The specific mass changes recorded during TGA of C19 and NIM 105 at 800 °C for 100 hours after pre-oxidation at 1100 °C for 1 hour are presented in Figure 10. The final specific mass changes for both C19 and NIM 105 are approximately 0.0050 and 0.0075 mg/cm², respectively. Note that the magnitude of the specific mass changes is on the order of μg as opposed to mg seen previously in Figure 2. Oscillations associated with day/night temperature variations within the laboratory are apparent in both sets of data.

For greater clarity, the cumulative specific mass change effects with both the pre-oxidation treatment at 1100 °C for 1 hour and the subsequent exposure at 800 °C for 100 hours for C19 and NIM 105 are presented in Figure 11 and compared with the baseline experiment at 800 °C for 100 hours. The final specific mass changes for C19 and NIM 105 after pre-oxidation are much greater than the final specific mass changes of the baseline experiment. However, subsequent oxidation
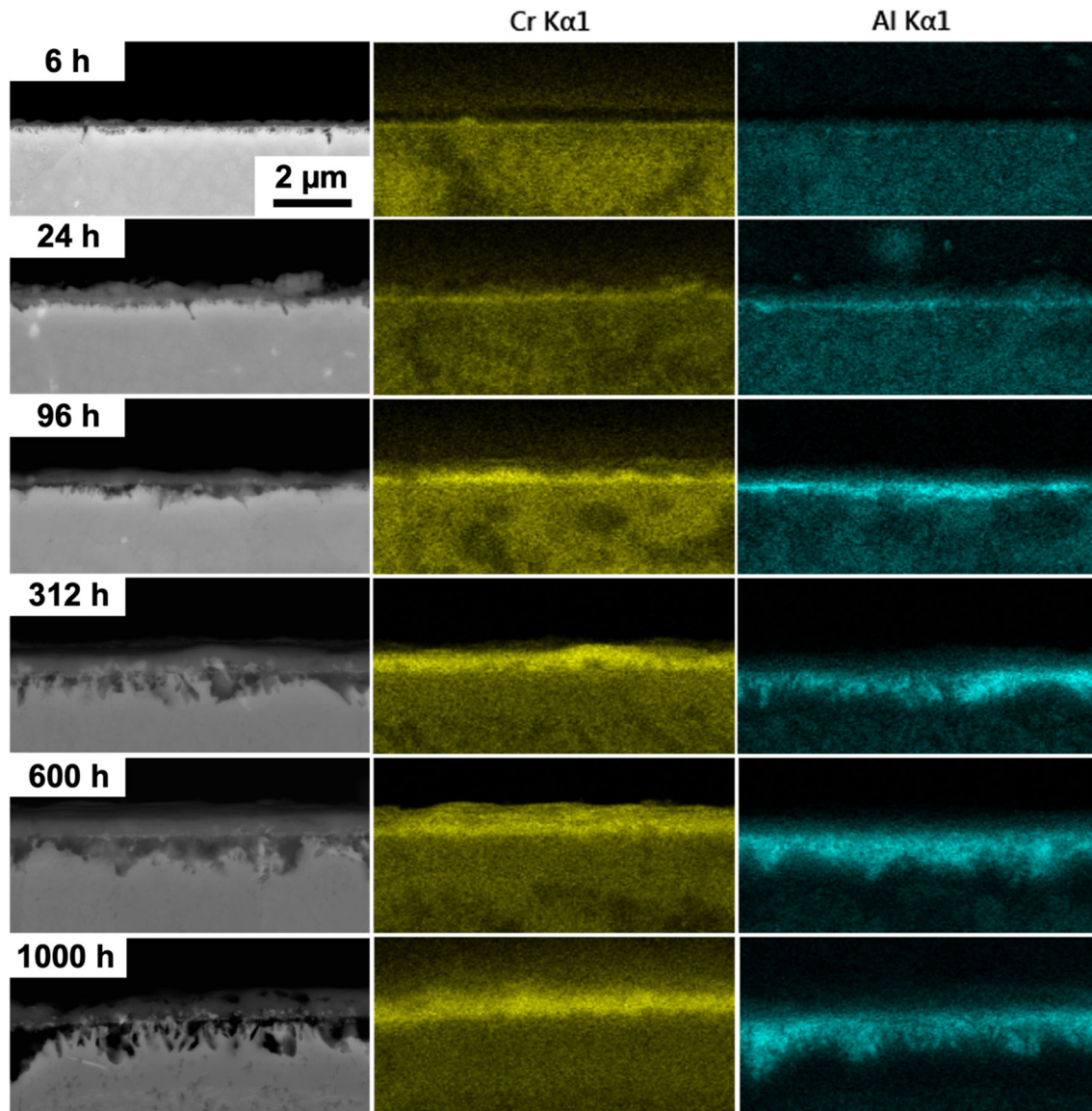
Fig. 6—Representative BSE SEM images of C19 cross sections at 800 °C after exposure to air for 6, 24, 96, 312, 600, and 1000 h (left). Corresponding EDX elemental concentration maps for Cr (yellow) and Al (blue) are provided to the right of the BSE SEM images (Color figure online).

of the pre-oxidized samples is virtually negligible and nearly invariant with time at 800 °C, as evidenced by the approximately flat-line profiles.

BSE micrographs and EDX elemental concentration maps at increasing magnifications for C19 and NIM 105 after pre-oxidation treatment at 1100 °C for 1 hour followed by 800 °C for 100 hour are presented in Figure 12. Similar to the results seen after the initial pre-oxidation exposure at 1100 °C, C19 exhibited a thin and continuous layer of Al_2O_3 throughout the entire cross-sectional surface, whereas NIM 105 showed Al_2O_3 intrusions underneath a prominent Cr_2O_3 scale. Note that the oxide-scale thickness in C19 (2.5 μm) is approximately half of the oxide-scale thickness in NIM 105 (5 μm). Occasional nodules of complex multi-layered oxides were observed along the surface of both C19 and NIM 105 but were much fewer in the former.

IV. DISCUSSION

A. Oxidation at 800 °C

The uniform oxide formation seen in Figure 3 suggests that the oxidation behavior of C19 at 800 °C occurs gradually with the formation of a continuous oxide front. Critically, there do not appear to be any specific regions of faster-growing oxides present on the surfaces, which have been observed at grain boundaries in similar alloys.[35] This is consistent with the TGA data obtained at this temperature, which showed progressive increases in specific mass change for C19 as well as NIM 105. The TGA-specific mass change for NIM 105 is in good agreement with previously published results at 850 °C.[36] The mass gain exponent, n, for C19 was 2.423 (Table II), suggesting oxide growth kinetics between parabolic and cubic, while that of NIM 105 was 1.915,

which is indicative of classic parabolic behavior. These differences in mass gain exponent values suggest different oxidation mechanisms are operative in these alloys. Notably, the k_n value for C19 was an order of magnitude lower than that of NIM 105 and the final specific mass change from oxidation at 800 °C in air for C19 (0.08 mg/cm^2) is significantly lower than the final specific mass changes reported for RR1000 at 800 °C (0.2 to 0.3 mg/cm^2).[35,37] The relatively low specific mass change at 800 °C in C19 suggests that it exhibits superior oxidation resistance to RR1000.

The parabolic growth rate of an oxide scale is typically attributed to the solid-state diffusion of species through a single scale.[28] However, C19 and NIM 105 produced compound scales consisting of more than one oxide, which can be particularly observed in Figures 5, 9, and 12. Therefore, it is noted that the n and k_n coefficients in this study should be interpreted as holistic values rather than those representative of individual oxide species. In contrast, the instantaneous oxidation rate constants might be more suitable indicators for tracking the growth of individual oxide scales. However, the holistic values for n and k_n still provide a reasonably quantitative means for overall comparisons of oxidation behavior between C19 and NIM 105.

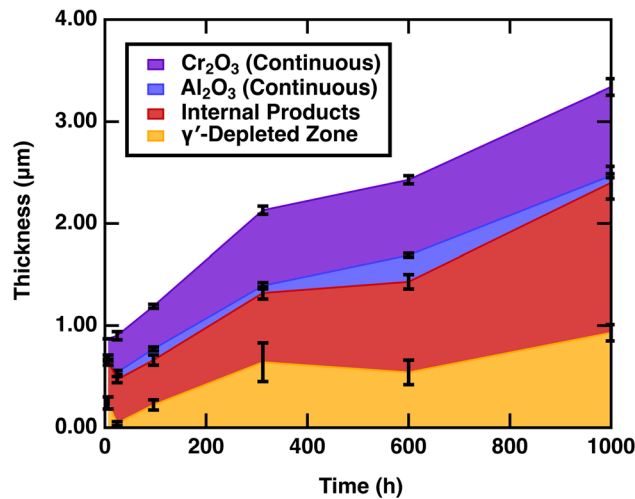In the XRD results from C19 following oxidation at 800 °C for 1000 hours, Figure 4, peaks from the

expected oxides of Cr_2O_3 and Al_2O_3 were identified along with peaks associated with TiO_2, $NiCr_2O_4$, and $MnCr_2O_4$. The presence of these phases was supported by the BSE and EDX images in Figure 5. For superalloys with similar compositions to C19, a variety of oxides including spinels (AB_2X_4), rutiles, and tri-rutiles (AB_2X_6, tapiolites) have been previously reported.[38,39] In particular, the presence of TiO_2 has been associated with detrimental oxidation resistance[5] while other phases, such as $NiTa_2O_6$, have been shown to improve or have negligible effects on oxidation resistance.[38] In C19, there was no direct evidence of tri-rutile formation but the presence of TiO_2 did not appear to cause excessive oxidation. This could be due to the significantly lower concentration of Ti in C19 relative to other polycrystalline superalloys,[5] which would result in reduced TiO_2 formation. Despite the dominance of Cr_2O_3 in the external scale, Figure 5 also shows there were specific regions of the oxidized C19 surface where a near-continuous Al_2O_3 scale formed. It is hypothesized that these regions were formed from the gradual coalescence of the Al_2O_3 fingers, which suggests that C19 has marginal Al_2O_3-forming capability at 800 °C.

The internal oxidation of Al in C19 during oxidation at 800 °C in Figure 6 is relatively slow, appearing primarily as internal particles that increase in size horizontally (parallel to the surface) and vertically (perpendicular to the surface) with time, with the latter direction being more prominent. Continuous scales of Al_2O_3 were only observed in specific, isolated regions. However, a discontinuous but sizeable subscale of Al_2O_3

Fig. 7—Thickness values (μm) measured in C19 following oxidation at 800 °C for Cr_2O_3, Al_2O_3, internal products, and γ'-depleted layers. Results are cumulatively stacked and presented in order of increasing exposure time from 6 to 1000 h.
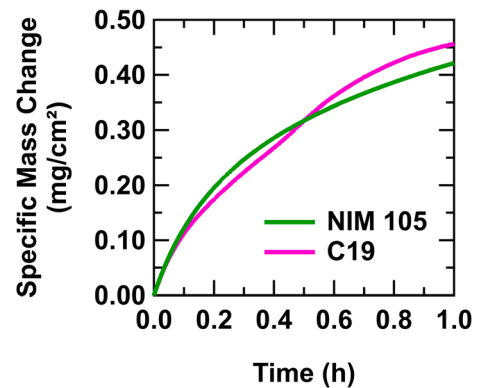

Fig. 8—TGA specific mass change curves for C19 and NIM 105 during pre-oxidation at 1100 °C for 1 h in air.

Table III. Calculated Minimum Critical Concentration of Al Required for External Oxidation at 800 °C for C19 with Eq. [1] and the Associated Variable Values Used

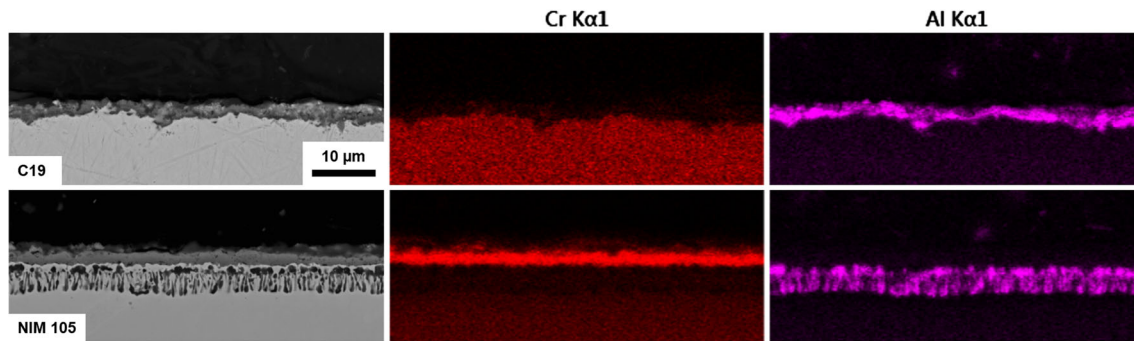| Method of Calculating D_B	V_m (cm^3/mol)	N_O^S (at. fr.)	D_O (cm^2/s)	D_B (cm^2/s)	N_B^o (at. pct)	x_{Al} (at. pct)
Allison and Samelson[31]	7.27	1.75×10^{-4}	7.07×10^{-10}	8.34×10^{-10}	11.5	9.4
Thermo-Calc 2021b TCNi8 v8.2 and MOBNi3 v3.2[34]	7.27	1.75×10^{-4}	7.07×10^{-10}	1.59×10^{-12}	8.3	9.4

Fig. 9—Cross-sectional BSE SEM images and EDX elemental concentration maps of Cr and Al for C19 and NIM 105 following pre-oxidation in air at 1100 °C for 1 h.
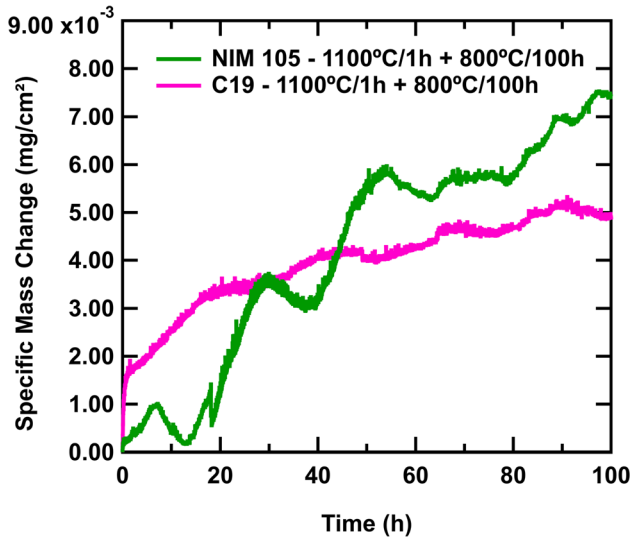

Fig. 10—TGA specific mass change curves for C19 and NIM 105 after pre-oxidation at 1100 °C for 1 h + 800 °C for 100 h in air.
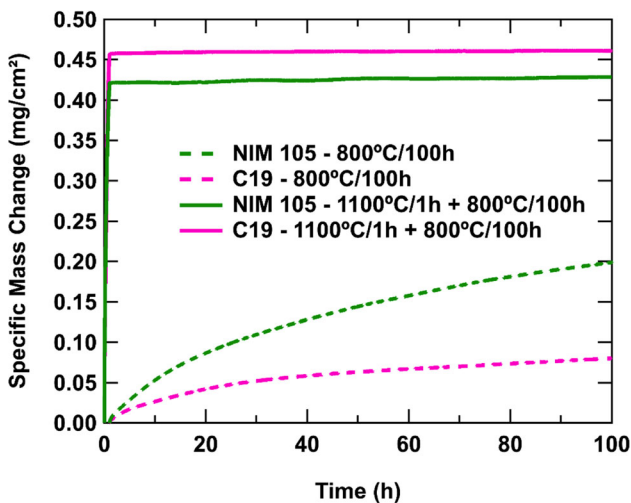

Fig. 11—Cumulative TGA specific mass change curves for C19 and NIM 105 after exposure at 800 °C for 100 h with and without pre-oxidation at 1100 °C for 1 h.

was nonetheless formed, the onset of which is visible after 96 hours and is supported by the results in Figure 7 where a significant increase in the thicknesses of the internal products (Al_2O_3 intrusions) was observed. After longer times (600 and 1000 hours), the growth of Al_2O_3 intrusions appears to be mostly in the vertical direction and penetrates further into the substrate resulting in the well-known Al_2O_3 fingers morphology. These results are in general agreement with classical oxidation behavior of Type II Ni–Cr–Al alloys as reported by Giggins and Pettit.[1] However, the isolated regions of continuous Al_2O_3 scales throughout the cross section suggest that the composition of C19 is close to a threshold where continuous Al_2O_3 formation may be achieved. This is in contrast to NIM 105 which does not show such behavior. This is interesting as C19 contains lower concentrations of both Al and Cr than NIM 105. It is, therefore, not possible to ascribe the behavior of C19 to Al and Cr contents alone. However, the increased propensity of C19 in forming a continuous scale of Al_2O_3 can potentially be attributed to two main compositional differences relative to NIM 105. First, C19 has a significantly higher concentration of Mn (0.59 at. pct) compared to NIM 105 (0.02 at. pct). The beneficial effect of this element on oxidation resistance has been reported by several other researchers,[40–42] with Mn dramatically reducing the specific mass changes. While the exact mechanisms are unclear, a similar study on a polycrystalline Ni-based superalloy at 800 °C found that Mn forms a protective spinel of $MnCr_2O_4$ that alternates with Cr_2O_3 layers to form a relatively protective compound scale.[41] It is possible that the combination of $MnCr_2O_4$ and Cr_2O_3 scales provides a more effective barrier against further penetration of oxygen, thereby allowing more time for Al to form a continuous Al_2O_3 scale. As a result, it is reasonable to attribute the superior capability of C19 to form Al_2O_3 due to its larger Mn concentration when compared to NIM 105. It is also possible that the significantly lower concentration of Mo, known for adversely affecting oxidation resistance, in C19 (1.79 at. pct) compared to NIM 105 (2.93 at. pct) could also be contributing to the enhanced oxidation behavior. It has been reported[43] that Mo promotes the internal oxidation of Al, which could further explain why C19
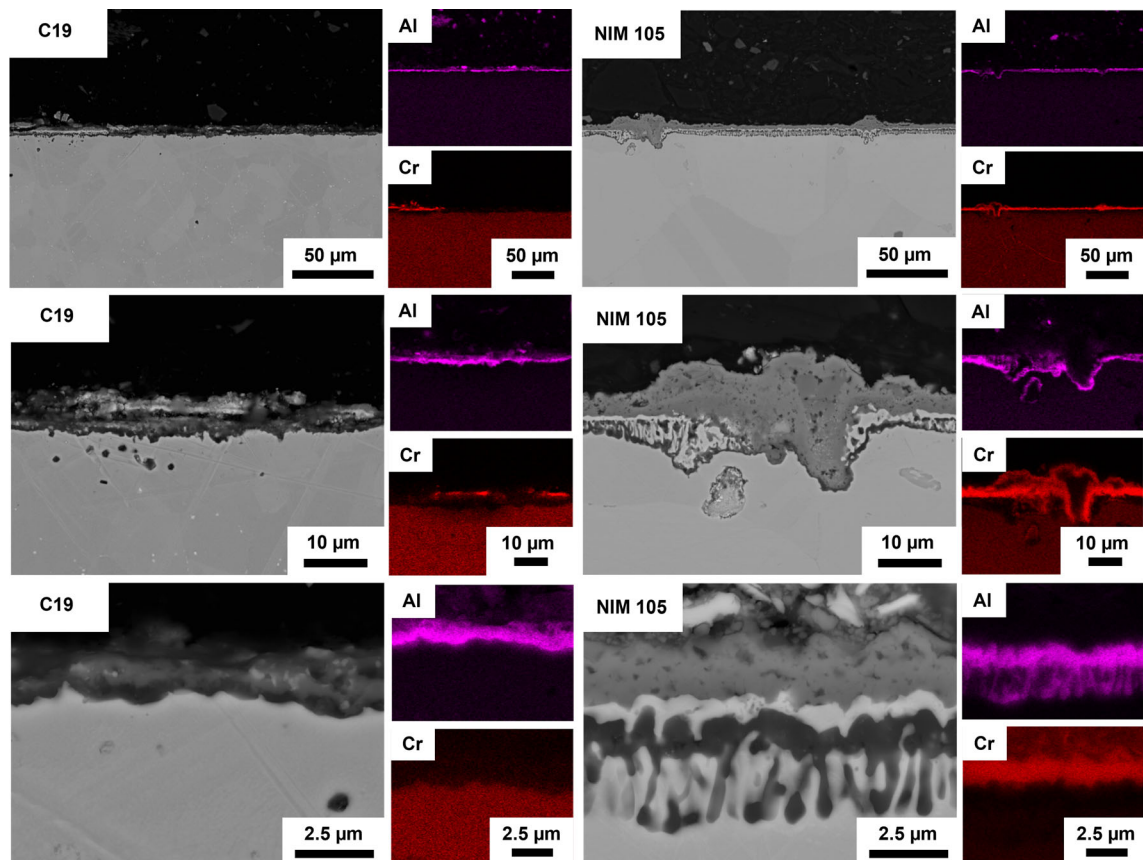
Fig. 12—BSE SEM micrographs of C19 and NIM 105 after pre-oxidation treatment at 1100 °C for 1 h followed by exposure at 800 °C for 1000 h. EDX elemental concentration maps for Al and Cr are shown alongside the BSE SEM micrographs. C19 demonstrates a continuous Al_2O_3 scale. NIM 105 exhibits a predominately Cr_2O_3 scale with distinct Al_2O_3 finger-like intrusions.

achieved Type III behavior as opposed to NIM 105, which remained a Type II alloy.

The depth of the Al_2O_3 intrusions in C19 after 1000 hours of oxidation reached a limiting value of ~ 1 to 2 μm, which is much lower than previously reported results for RR1000 after oxidation at 800 °C for 1000 hours, which exhibited internal oxide depths of ~ 10 μm and total oxidation damage depths of ~ 10 to 20 μm.[8] Oxide damage depths up to 5 μm have also been reported for RR1000 following exposure at 750 °C for 1000 hours.[44] In C19, the mean total depth of the oxidation damage is approximately 3.3 μm, which is considerably lower than those observed in similar alloys after accounting for temperature.[5,8,44] By cross-examining the measured thicknesses and specific mass changes of C19 with the literature, it appears that C19 has the potential of outperforming several commercial turbine disk alloys and effectively offering an improvement in oxidation temperature capability of approximately 50 °C.

B. The Effect of Pre-oxidation

During the pre-oxidation treatment of 1 hour at 1100 °C, large specific mass changes were observed in C19 and NIM 105 (Figure 8). This can be rationalized with reference to Eqs. [2] through [4], which predict that the solubilities and diffusivities of both oxygen and Al increase markedly with temperature. NIM 105 exhibits parabolic behavior from the onset while C19 only establishes parabolic behavior at the 0.5 hour mark, suggesting that C19 is slower at establishing a passivating oxide layer than NIM 105 at 1100 °C. Importantly, the specific mass changes at 800 °C for 100 hours after pre-oxidation at 1100 °C for 1 hour are comparatively lower than in other studies. For example, a similar study[17] on Nimonic 95 reported specific mass changes that were several orders of magnitude higher (approximately 2 mg/cm^2) than the findings in this study. This could potentially be due to that study having conducted pre-oxidation at 800 °C for 140 hours which would result in an environment that has been shown to preferentially form Cr_2O_3.[45] Further comparisons can be made with the oxidation performance of alloys that are known to be Al_2O_3 formers at high temperature. For comparison, the specific mass change of the second-generation single-crystal Ni-based superalloy CMSX-4 at 1100 °C for 1 hour in air has been reported to be approximately 0.15 mg/cm^2,[46] which is nearly one third of the specific mass changes observed for C19 (0.45 mg/cm^2) and NIM 105 (0.42 mg/cm^2). This difference in oxidation performance under the same conditions is to be expected given the higher Al content in CMSX-4 compared with C19 and NIM 105. However, the specific

mass change of the third-generation single-crystal Ni-based superalloy CMSX-10 at 1100 °C for 1 hour in air has been reported to be approximately 1.5 mg/cm^2,[47] which is nearly three times higher than the specific mass changes measured for C19 and NIM 105 under the same conditions. The relatively poor oxidation performance of CMSX-10 has been attributed to its exceptionally low Cr concentration (2.4 at. pct) and the formation of complex oxides instead of Al_2O_3[22], further highlighting the importance of both Al and Cr in providing desirable oxidation resistance.

It is apparent from Figure 11 that the specific mass changes of C19 and NIM 105 are substantial during the pre-oxidation treatment and several times larger than in the baseline experiment. It is also observed that NIM 105 exhibits a slightly lower specific mass change than C19 in the pre-oxidized condition, which contradicts the baseline experiment where NIM 105 showed a significantly larger specific mass change than C19. This could be explained by the results observed in Figure 8 where NIM 105 instantly exhibits a parabolic curve while C19 begins parabolic behavior only from approximately 0.5 hour onward, suggesting that C19 is slower than NIM 105 in forming an initial continuous and protective oxide layer. This phenomenon is also consistent with Figure 10 where the specific mass change for C19 appears to flatten with increasing time while NIM 105 exhibits a continuously increasing specific mass change. This suggests that C19 ultimately forms a more continuous and protective Al_2O_3 layer during the period at 1100 °C (Figure 9) at the expense of a slightly larger mass gain by the end of the pre-oxidation treatment whereas NIM 105 forms a less protective Cr_2O_3 layer that results in a continued increase in specific mass change.

The cross-sectional micrographs from C19 and NIM 105 after exposure at 1100 °C for 1 hour and then after a further 100 hours at 800 °C in Figure 12 show significantly different oxide morphologies. C19 formed a thin and continuous layer of Al_2O_3 throughout the entire cross-sectional surface, which is consistent with Type III oxidation behavior.[1] In contrast, NIM 105 showed Al_2O_3 intrusions underneath a prominent Cr_2O_3 scale which agrees with previously reported results of NIM 105[36] and is typical of Type II oxidation behavior. These results also support the TGA results in Figure 10 where specific mass changes are two orders of magnitude lower than the baseline experiment in Figure 2 and provide evidence of virtually complete passivation in both alloys. It is particularly noted that these morphologies were established immediately after pre-oxidation at 1100 °C for 1 hour in Figure 9 and do not evolve significantly with further exposure at 800 °C. This observation is corroborated by Figure 10 which shows that the specific mass changes of C19 and NIM 105 are on the same order of magnitude as the noise-level oscillations of the equipment.

While the cross section of the C19 alloy primarily demonstrated a sole Al_2O_3 scale, there were some isolated regions of the surface that showed relatively complex and fragmented scales (left-top and left-center insets of Figure 12). While these regions were not representative of the cross section, their description is included to ensure a comprehensive analysis. EDX analysis showed the presence of Ni, Co, Mo, and Cr in the top-most stratum of the scale while an enrichment of Ti, Ta, Nb, and Mn was detected in the intermediate stratum. It is possible that the enhanced kinetics at 1100 °C facilitated the growth of these complex oxides during a period of transient oxidation. However, a strong presence of a continuous Al_2O_3 layer was observed underneath these complex oxides, suggesting that the complex oxides may have reduced the rate of oxygen ingress in these areas to allow for a protective layer of Al_2O_3 to be established within 1 hour. While few, the presence of such regions of complex oxides could suggest that the choice of pre-oxidation temperature and duration requires further detailed investigation. However, a homogeneous Al_2O_3 layer was consistently observed throughout the examined cross sections, which supports the hypothesis that pre-oxidation resulted in adequate passivation of the alloy.

Overall, the results suggest that the oxidation behavior of C19 is more favorable than NIM 105 without and with pre-oxidation treatment. This behavior has arisen despite C19 containing lower concentrations of both Al and Cr than NIM 105. Similar to the baseline experiments at 800 °C, the greater concentration of Mn in C19 could work synergistically with Cr to limit oxygen ingress and facilitate formation of a continuous Al_2O_3 layer. Specifically, at 1100 °C, faster rates of diffusion are expected than at 800 °C and as such, the $MnCr_2O_4$/ Cr_2O_3 scale is more readily formed at the alloy–air interface. This reduces oxygen ingress into the substrate such that Al may more readily diffuse to the metal–oxide interface. This could explain why C19 succeeds in forming a continuous Al_2O_3 layer. In contrast, NIM 105 does not have significant amounts of Mn and, therefore, relies mostly on its greater Cr concentration to form a Cr_2O_3 scale, which is not as protective and allows oxygen to diffuse deeper into the substrate and precipitate Al_2O_3 "finger-like" intrusions. Therefore, it is highly possible that the increased presence of Mn in C19 ensures its improved defense against initial oxygen partial pressures despite its slightly larger Ti concentration. However, further experiments would be needed to fully understand the oxidation dynamics between Mn–Cr–Ti. The higher amount of Mo in NIM 105 may also contribute to its inferior oxidation behavior as Mo has been shown[43] to adversely affect oxidation resistance. Due to the complex compositions of both C19 and NIM 105, further detailed investigations would be required to unambiguously isolate and assess the contributions of each element toward oxidation performance.

While the pre-oxidation treatment improves the passivating capabilities of both alloys, the oxidation resistance of NIM 105 appears to rely on a primary Cr_2O_3 scale at both 800 °C and 1100 °C. It is, therefore, hypothesized that the continuous Al_2O_3 scale formed in C19 would be the better option for higher temperature operation. To the knowledge of the authors, this is the first instance of applying a high-temperature (1100 °C) pre-oxidation regime to instigate the transition from

Cr_2O_3-forming to Al_2O_3-forming behavior in a polycrystalline Ni-based superalloy. There are several aspects of the pre-oxidation treatment that could be further optimized, including the pre-oxidation temperature, and duration as well as the predictive fidelity of the Wagner model. It is accepted that the incorporation of such an oxidation pre-treatment may present challenges for component manufacture, but may conceivably be incorporated into production schedules before precipitate solutioning and aging treatments. The resilience/damage tolerance of an Al_2O_3 scale formed by a pre-oxidation treatment and its subsequent regeneration capability under service conditions would also need to be further investigated.

V. CONCLUSIONS

The oxidation behavior of a new polycrystalline Ni-based superalloy (C19) has been studied in air at 800 °C for up to 1000 hours. The main findings of this study are summarized as follows:

1. C19 formed a continuous external Cr_2O_3 scale early in the oxidation process in air at 800 °C accompanied by internal Al_2O_3 finger-like intrusions, characteristic of Type II oxidation behavior. Isolated regions of continuous Al_2O_3 were also observed.
2. The oxidation performance of C19 at 800 °C was benchmarked against NIM 105 and shown to be similar to established Cr_2O_3-forming polycrystalline turbine disk alloys exposed to air at 750 °C for 1000 hours, potentially offering improved oxidation resistance.
3. Wagner oxidation theory calculated that the Al concentration of C19 was inadequate to form a continuous Al_2O_3 scale but close to the transition point between Cr_2O_3-forming and Al_2O_3-forming behavior.
4. Pre-oxidation treatment at 1100 °C for 1 hour resulted in the formation of a continuous and protective Al_2O_3 scale in C19, suggesting a transition to Type III oxidation behavior. During subsequent exposure at 800 °C for 100 hours, minimal specific mass changes were observed. NIM 105 failed to form a continuous Al_2O_3 scale with the same pre-oxidation treatment.

CONFLICT OF INTEREST

On behalf of all authors, the corresponding author states that there is no conflict of interest.

OPEN ACCESS

REFERENCES

1. C. Giggins and F. Pettit: *J. Electrochem. Soc.*, 1971, vol. 118, pp. 1782–90.
2. B.W. Lagow: *JOM*, 2016, vol. 68, pp. 2770–75.
3. T. Sand, J. Liske, T. Helander, J.E. Svensson, and L.G. Johannson: *Oxid. Met.*, 2022, vol. 98, pp. 163–78.
4. B. Jönsson and A. Westerlund: *Oxid. Met.*, 2017, vol. 88, pp. 315–26.
5. J.H. Chen, P.M. Rogers, and J.A. Little: *Oxid. Met.*, 1997, vol. 47, pp. 381–410.
6. A. Chyrkin, P. Huczkowski, V. Shemet, L. Singheiser, and W.J. Quadakkers: *Oxid. Met.*, 2011, vol. 75, pp. 143–66.
7. K.A. Christofidou, N.G. Jones, M.C. Hardy, and H.J. Stone: *Oxid. Met.*, 2016, vol. 85, pp. 443–58.
8. S. Cruchley, M.P. Taylor, H.E. Evans, M.C. Hardy, and D.J. Child: *Mater. Sci. Technol.*, 2014, vol. 30, pp. 1884–89.
9. F. Ismail, V. Vorontsov, T. Lindley, M. Hardy, D. Dye, and B. Shollock: *Corros. Sci.*, 2017, vol. 116, pp. 44–52.
10. F. Gesmundo: *Mater. Sci. Forum*, 1997, vol. 251–254, pp. 3–18.
11. T. Perez, D. Monceau, and C. Desgranges: *Corros. Sci.*, 2022, vol. 206, pp. 1–3.
12. L.S. Darken: *Trans. Am. Inst. Min. Metall. Pet. Eng.*, 1942, vol. 150, pp. 157–69.
13. C. Wagner: *Z. Elektrochem.*, 1958, vol. 63, pp. 772–82.
14. R.A. Rapp: *Acta Metall.*, 1961, vol. 9, pp. 730–41.
15. J.A. Nesbitt: *J. Electrochem. Soc.*, 1989, vol. 136, pp. 1518–527.
16. F. Abe, H. Kutsumi, H. Haruyama, and H. Okubo: *Corros. Sci.*, 2017, vol. 114, pp. 1–9.
17. D. Li, J. Chen, I.P. Etim, Y. Liu, C. Wu, J. Wang, and X. Su: *Vacuum*, 2021, vol. 194, 110582.
18. S. Mathieu, L. Aranda, L. Portebois, S. Mathieu, and M. Vilasi: *Oxid. Met.*, 2018, vol. 90, pp. 43–63.

19. M.C. Hardy, K. Christofidou, P.M. Mignanelli, H.J. Stone, N.G. Jones, and C. Argyrakis: Patent No. US 2019/0360077, November 28, 2019.
20. M.C. Hardy, K. Christofidou, P.M. Mignanelli, H.J. Stone, N.G. Jones, and C. Argyrakis: Patent No. US 2019/0360078, November 28, 2019.
21. K. Kawagishi, A. Sato, T. Kobayashi, and H. Harada: *J. Jpn. Inst. Met.*, 2007, vol. 71, pp. 313–19.
22. A. Akhtar, M.S. Hook, and R.C. Reed: *Metall. Mater. Trans. A*, 2005, vol. 36A, pp. 3001–17.
23. M. Bensch, A. Sato, N. Warnken, E. Affeldt, R.C. Reed, and U. Glatzel: *Acta Mater.*, 2012, vol. 60, pp. 5468–80.
24. A. Sato, J.J. Moverare, M. Hasselqvist, and R.C. Reed: *Metall. Mater. Trans. A*, 2012, vol. 43A, pp. 2302–15.
25. J.J. Schirra, R.H. Caless, and R.W. Hatala: *International Symposium on Superalloys 718, 625 Various Derivatives*, 1991, pp. 375–88.
26. J.D. Donaldson and S.J. Clark: *Cobalt in Superalloys*, Strobel and Sons, London, 1985.
27. R.C. Reed: *The Superalloys: Fundamentals and Applications*, Cambridge University Press, Cambridge, 2006.
28. D.J. Young: *High Temperature Oxidation and Corrosion of Metals*, 1st ed. Elsevier, Amsterdam, 2008.
29. J.W. Park and C.J. Altstetter: *Metall. Mater. Trans. A*, 1987, vol. 18A, pp. 43–50.
30. H.W. Allison and H. Samelson: *J. Appl. Phys. (Melville, NY, U. S.)*, 1959, vol. 30, pp. 1419–24.
31. F.S. Pettit: *Trans. Metall. Soc. AIME*, 1967, vol. 239, pp. 1296–305.
32. W. Zhao, Y. Kang, J.M.A. Orozco, and B. Gleeson: *Oxid. Met.*, 2014, vol. 83, pp. 187–201.
33. J.O. Andersson, T. Helander, L. Höglund, P.F. Shi, and B. Sundman: *CALPHAD*, 2002, vol. 26, pp. 273–312.
34. M.P. Taylor, H.E. Evans, S. Stekovic, and M.C. Hardy: *Mater. High Temp.*, 2014, vol. 29, pp. 145–50.
35. J.B. Johnson, J.R. Nicholls, R.C. Hurst, and P. Hancock: *Corros. Sci.*, 1978, vol. 18, pp. 527–41.
36. A. Encinas-Oropesa, G.L. Drew, M.C. Hardy, A.J. Leggett, J.R. Nicholls, and N.J. Simms: *11th International Symposium on Superalloys*, 2008, pp. 609–18.
37. C.A. Barrett, R.V. Miner, and D.R. Hull: *Oxid. Met.*, 1983, vol. 20, pp. 255–78.
38. C.A. Barrett: Report No. 87297, NASA, March 1986.
39. S. Pedrazzini, D. Child, G. West, S. Doak, M. Hardy, M. Moody, and P. Bagot: *Scr. Mater.*, 2016, vol. 113, pp. 51–4.
40. E. Anzini, N. Glaenzer, P.M. Mignanelli, M.C. Hardy, H.J. Stone, and S. Pedrazzini: *Corros. Sci.*, 2020, vol. 176, 109042.
41. D. Douglass and J. Armijo: *Oxid. Met.*, 1970, vol. 2, pp. 207–31.
42. S.J. Park, S.M. Seo, Y.S. Yoo, H.W. Jeong, and H.J. Jang: *Materials*, 2019, vol. 12, p. 2934.
43. A. Encinas-Oropesa, N.J. Simms, J.R. Nicholls, G.L. Drew, J. Leggett, and M.C. Hardy: *Mater. High Temp.*, 2009, vol. 26, pp. 241–49.
44. X.G. Zheng and D.J. Young: *Oxid. Met.*, 1994, vol. 42, pp. 163–89.
45. H.T. Pang, F. Li, S. Pahlavanyali, I.M. Edmonds, G. Brewster, and C.M.F. Rae: *13th International Symposium on Superalloys*, 2016, pp. 949–58.
46. R.H. Perry: *Perry's Chemical Engineers' Handbook*, 7th ed. McGraw-Hill, New York, 1997.
47. S.R. Hegde: *Master of Applied Science Thesis*, University of British Columbia, Vancouver, 2005.